

Optimization of rear surface roughness and metal grid design in industrial bifacial PERC solar cells

H.B. Tang^a, S. Ma^{a,b}, Y. Lv^a, Z.P. Li^a, W.Z. Shen^{a,c,*}

^a Institute of Solar Energy, Key Laboratory of Artificial Structures and Quantum Control (Ministry of Education), Department of Physics and Astronomy, Shanghai Jiao Tong University, Shanghai, 200240, People's Republic of China

^b Sunin New Energy Development Co., Ltd., Nantong, 226331, People's Republic of China

^c Collaborative Innovation Center of Advanced Microstructures, Nanjing, 210093, People's Republic of China



ARTICLE INFO

Keywords:

Bifacial solar cell
Silicon
PERC
Surface morphology
Metal grid design

ABSTRACT

The bifacial *p*-type silicon (*p*-Si) passivated emitter and rear cells (PERCs) are predicted to dominate the industrial bifacial solar cells. In this work, we have investigated the impact of different rear surface morphologies on the electrical performance of bifacial PERCs with both five-busbar (5BB) and nine-busbar (9BB) grid design. The passivation and optical properties with differing rear surfaces are evaluated on semi-device structures. The depth of local aluminum back surface field is hardly affected by the rear surface morphology. The calculated efficiency loss analysis indicates that the negative electrical impact with enlarged rear surface area is more serious for rear side than that of front side. The batch conversion efficiency of 9BB bifacial PERCs increases by 0.2%–0.3% comparing to 5BB ones depending on the rear surface roughness. Consequently, a highest front-side average efficiency of 22.57%, with a champion efficiency of 22.75%, has been achieved for 9BB bifacial *p*-Si PERCs with a nearly planar rear surface. A highest bifaciality of 78.7% is realized for both 5BB and 9BB bifacial PERCs with the roughest rear surface. We have further simulated the relative enhancement of electric generation to compare the performance of bifacial PERCs in practical application.

1. Introduction

Recently, the crystalline silicon (c-Si) passivated emitter and rear cells (PERCs) have dominated the highly competitive photovoltaic market due to low industrial cost, simple manufacturing process and high power conversion efficiency (η) [1–3]. The average efficiency for mass produced Czochralski (Cz) *p*-type Si based PERCs has stepped into the stage of 22.5% and LONGi solar declared the world-record efficiency of PERCs to be 24.06% in 2019 [4]. The annual production capacity of *p*-Si PERCs has already reached over 100 GWp in 2019 in China. Another advantage of the *p*-Si PERCs is the easy processing sequence and the fabrication of bifacial solar cells are fully compatible with existing PERC production lines only by replacing full area aluminum back surface field (Al-BSF) with Al finger grids on the rear side [5,6]. The amount of consumed Al paste has been proved to be dramatically reduced by 90% and deeper *p*⁺-doped Al-BSF can be yielded for higher open-circuit voltage (V_{oc}) [7].

As we know, bifacial solar cells have received extensive attention [8,

9] because of their potential to absorb sunlight from the front side and rear side simultaneously, which was predicted to increase the annual produced electricity by up to 30% [10,11], thus causing the reduction of the levelized cost of electricity. Such a concept was first proposed by Mori in 1960s [12], but bifacial solar cells were transferred into mass production in recent years driven by mature passivation technology [13, 14], high conductive metal paste [15,16] and advanced laser ablation technology [17]. According to the International Technology Roadmap for Photovoltaic (ITRPV) 2020 [18], the market share of bifacial solar cells in 2019 was about 20% and predicted to increase to 70% in 2030. However, the typical *n*-type silicon bifacial solar cells, such as *n*-PERT (passivated emitter, rear totally diffused) [19,20] and HIT (heterojunction with intrinsic thin layer) [21,22], still encounter the challenge of low market share (only ~5 GWp in 2019) and significant high amount of silver paste due to the bifacial screen-printed silver finger grids, despite the bifaciality factor can be higher than 90%.

Dullweber et al. [7], pioneered the bifacial *p*-Si PERCs (PERC + concept) with front-side and rear-side efficiency of 20.8% and 16.5%,

* Corresponding author. Institute of Solar Energy, and Key Laboratory of Artificial Structures and Quantum Control (Ministry of Education), Department of Physics and Astronomy, Shanghai Jiao Tong University, Shanghai, 200240, People's Republic of China.

E-mail address: wzshen@sjtu.edu.cn (W.Z. Shen).

respectively, i.e., a bifaciality of 79.3%. By application of selective emitter and double-printed rear Al electrode, Wu et al. [23], reported in the literature the best front-side efficiency of 22.0% in bifacial *p*-Si PERCs so far, but with a low rear-side efficiency of 15.3%, a corresponding bifaciality of 69.5%. The lower bifaciality in bifacial *p*-PERCs comparing to that of bifacial *n*-PERT or HIT is mainly attributed to the nearly one fourth lower short-circuit current density (J_{sc}) value of rear-side [7,23], which is further limited by the inferior light-trapping property of polished rear surface in combination with high metallization shading fraction of rear Al grids [7]. A planar rear surface was favorable in case of monofacial PERCs [24,25] due to improved internal long-wavelength reflection and superior passivation property, while a planar surface was detrimental for light trapping when light comes from the rear side in bifacial PERCs. The impact of rear surface morphology on the performance of bifacial PERCs has not been investigated in detail.

On the other hand, numerous researches have put focus on the optimization of rear Al finger grids, including laser contact opening (LCO) width, finger printing width and pitch of fingers. Kranz et al. [26], demonstrated that narrower rear Al contact width would lead to deeper Al-BSF, thus lowered contact recombination loss and improved V_{oc} values in bifacial PERCs. Dullweber et al. [27], also showed that narrower LCO width had advantage in enhancing long wavelength reflectance and reducing the rear contact recombination due to reduced contact area. A contact width of $32 \pm 2 \mu\text{m}$, a finger opening width of $100 \mu\text{m}$ and a finger pitch of 1 mm were suggested considering the trade-off between the series resistance loss and rear shading area [6,28]. Meanwhile, the above works all adopted five-busbar (5BB) design for metal grid, the busbars also account for large shading fraction and series resistance loss. The market share of 5BB was predicted to decrease in the following ten years and replaced by multiple-busbar (MBB) technology [18,29,30]. The MBB technology was also confirmed to have a larger tolerance of Al finger width in order to keep the Al finger series resistance below $0.05 \Omega \text{ cm}^2$ [29].

In this study, we have investigated the impact of rear surface morphology on the performance of bifacial *p*-type PERCs both experimentally and theoretically. The electrical and optical characteristics with variable rear surface textures were evaluated systematically. By

integrating these rear surfaces into bifacial PERCs, cells with both 5BB and nine-busbar (9BB) configuration for rear Al grids were successfully fabricated with suggested design [6,28]. Finally, a calculation of the relative enhancement of energy generation was conducted to compare the performance of bifacial PERCs with differing rear surface morphologies in practical application.

2. Experimental and simulation

2.1. Fabrication of bifacial PERCs

The *p*-type Cz-grown silicon wafers with a size of $158.75 \text{ mm} \times 158.75 \text{ mm}$, a thickness of $180 \pm 20 \mu\text{m}$ and a resistivity of $0.8\text{--}2.0 \Omega \text{ cm}$ were used in this work. Fig. 1(a) shows the industrial process to fabricate the bifacial PERCs. First, the wafers were treated with RCA cleaning and alkaline texturing. After that, the samples underwent a diffusion (DS-300C, S.C.) back to back with POCl_3 as diffusion source to form a homogeneous n^+ emitter with the sheet resistance of nearly $130 \Omega/\square$. The highly doped n^{++} area with a sheet resistance of $80 \Omega/\square$ was formed with driving the P atoms originated from phosphorous silicate glass (PSG) layer into Si by a laser-doping process (DR-AL-Y40, DR Laser). Then, the single-sided chemical etching was performed on the textured pyramids with mixed HF/HNO_3 solution by an inline industrial system (InOxSide, RENA). The detailed etching process started with the oxidation of Si to SiO_2 by HNO_3 , followed by the dissolution of SiO_2 as a result of reacting with HF. The mass fraction of used HF and HNO_3 solutions is 49% and 45%, respectively. To obtain different rear surface morphologies, the volume ratio of HF to HNO_3 solution was changed to adjust the tilt angle of pyramids. After etching, PSG layer was removed in HF solution, and the thermal oxidation process was carried out on the samples with O_3 to form the SiO_2 layer. The AlO_x layer prepared by the atomic layer deposition (ALD, Ideal Energy) was capped by triple SiN_x/Hs to passivate the rear surface of the *p*-type wafers. Here, the SiN_x/Hs with a thickness of 85 nm were deposited by plasma-enhanced chemical vapor deposition (PECVD, PD-405C, S.C.) with the precursor gases: silane and ammonia. Next, the rear passivation layers were patterned with laser (DR-AL-Y40, DR Laser) to obtain a line width of about $32 \mu\text{m}$,

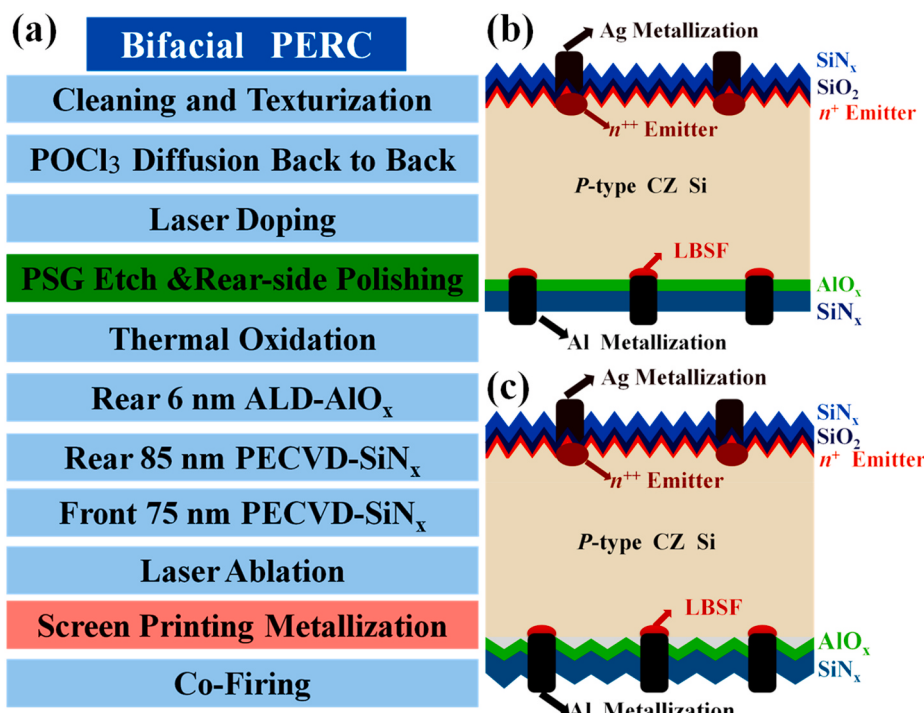


Fig. 1. (a) The industrial process for bifacial PERCs. Schematic structure of the fabricated bifacial *p*-Si PERCs with a (b) planar and (c) rough rear surface.

thus Al paste can diffuse into Si to form the local Al-BSF. Al screen-printing (Softline-DL-SP, Maxwell) was used to form the front and rear electrodes. Instead of the full area Al-BSF used in PERCs, the rear-side of bifacial PERCs applied an Al metal grid with a 5BB or 9BB design. With regard to the rear-side finger design, for both 5BB and 9BB, a printing width of 100 μm and a finger pitch of 1 mm were adopted as other researchers suggested [6,28], while the busbar width drops from 900 μm (5BB) to 400 μm (9BB). Finally, the fast sintering ($\sim 800^\circ\text{C}$ at peak temperature) was conducted in an infrared industrial belt-furnace (CFSeries, Despatch) to form the metal contacts and activate H atoms originated from $\text{SiN}_x:\text{H}/\text{AlO}_x$ layers. Fig. 1(b) and (c) show the schematic illustrations of fabricated bifacial PERCs with planar and rough rear surface, respectively.

2.2. Characterization

The three dimensional (3D) morphologies and roughness parameters of the etched samples were characterized by atomic force microscope (AFM, Nanonavi E-Sweep). The morphologies were also investigated by field emission scanning electron microscopy (FE-SEM, Zeiss Ultra Plus) to measure the pyramid facet angle. The resistivity of wafers and sheet resistance (R_{sh}) were tested by four-point probes (280I Series, Four Dimensions Inc.). The refractive index and thickness of AlO_x and SiN_x layers were determined by spectroscopic ellipsometry (SE400adv-PV) at $\lambda = 632\text{ nm}$. The reflectance and external quantum efficiency (EQE) of the solar cells were measured by PV Measurements system (QEX10). The transmittance spectra of the wafers were detected by Fourier transform infrared spectroscopy (FTIR, VERTEX 70, Bruker). Finally, the electrical parameters were measured under standard test conditions (AM 1.5G

spectrum, 25°C) by Halm 3600.

To investigate the influence of rear surface morphology on the passivation property, the effective minority carrier lifetime (τ_{eff}), implied open circuit voltage (iV_{oC}) and dark saturation current density (J_{0e}) of symmetrical structures were measured by a quasi-steady-state photoconductance method (WCT-120, Sinton Instruments) at an injection density of $1 \times 10^{15}\text{ cm}^{-3}$. After texturization, both sides of the wafers were polished with a similar single-sided etching process using mixed $\text{HF}/\text{HNO}_3/\text{H}_2\text{O}$ solution. Then stack of $\text{SiN}_x:\text{H}/\text{AlO}_x$ passivation layers were deposited symmetrically on both sides of the wafers with a $\text{SiN}_x:\text{H}/\text{AlO}_x/\text{Si}/\text{AlO}_x/\text{SiN}_x:\text{H}$ structure, followed by a high temperature annealing process in an industrial firing furnace.

2.3. Simulation

The impact of rear surface morphology on electrical performance of the bifacial PERC unit cell was simulated by PV Lighthouse software Quokka 2 [3,31,32], and free energy loss analysis (FELA) was extracted to understand the recombination loss and resistive loss of cells. Here, the electrical impact of different rear surface morphologies was represented by the varied value of rear passivated dark saturation current density J_0 , passivated when light comes from front side or rear side. The optical generation file applied in Quokka 2 was extracted from ray tracing simulator OPAL 2. It should be noted that the rear surface morphology also has a significant influence on optical characteristic. Meanwhile, it is difficult to accurately describe the morphology due to the rounding at peaks and valleys of etched pyramids (see Fig. 2). Therefore, when carrying out the OPAL 2 simulation, only the pyramid facet angle was changed without considering the rounding effect. The main simulation

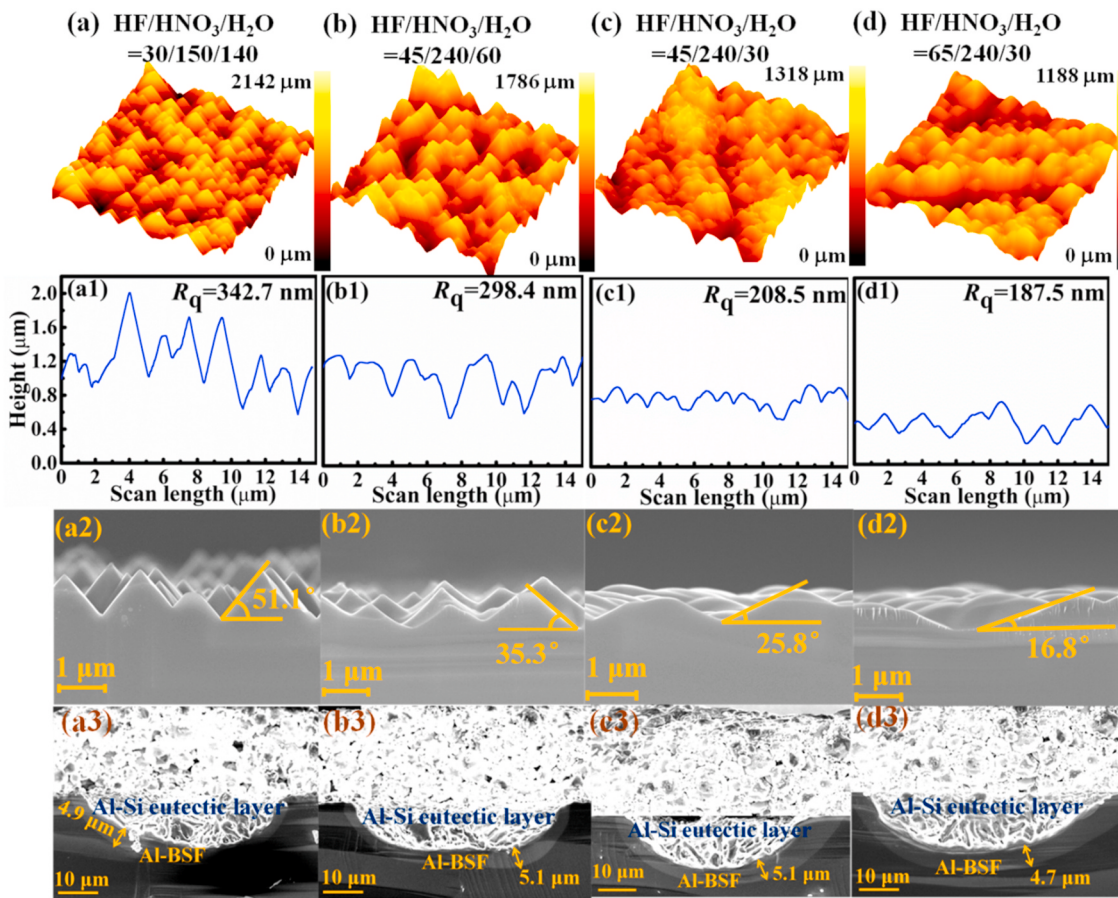


Fig. 2. (a-d) AFM images of the rear surface etched in four different acid solutions. (a1-d1) Height distribution and the root mean square R_q along a line on the surface. (a2-d2) Cross-sectional SEM images of the processed rear surface. (a3-d3) SEM images of the local aluminum silicon contacts. (For interpretation of the references to colour in this figure legend, the reader is referred to the Web version of this article.)

parameters were listed in Table 1.

To evaluate the performance of bifacial PERCs with different rear surface structures in practical application, the electric energy generation on, as an example, June 22nd was calculated based on the measured EQE spectra and the photon flux of solar irradiance spectra [33,34]. The solar irradiance spectra were extracted from solar spectrum calculator on online PV lighthouse software. The modules were assumed to locate in Shanghai (121° , 31°), with a tilt angle of 30° and azimuth angle of 180° (face due south).

3. Results and discussion

3.1. Morphology

After wet chemical etching, the morphologies and roughness parameters of the wafers were analyzed by AFM. Fig. 2(a–d) show the 3D topography of the rear surface prepared in etching solution with different volume ratios of HF/HNO₃/H₂O, all the images were scanned in a region with the scale of $15\text{ }\mu\text{m} \times 15\text{ }\mu\text{m}$. After etching in HF/HNO₃/H₂O solution at a volume ratio of 30/150/140 (Fig. 2(a)), the silicon surface is covered by uniformly distributed random pyramids. The height of pyramids decreases with increasing the concentration of HF and HNO₃ in Fig. 2(b), while the pyramid structure is still obviously visible. Further increasing the concentration of HF and HNO₃, smoothed pyramid peaks and troughs are observed in Fig. 2(c), this is ascribed to

the higher etching rate of pyramid peaks than that of pyramid valleys [35]. The smoothing effect is enhanced with higher proportion of HF solution, thus the nano-pyramids tend to disappear and combine to form the larger pyramids in Fig. 2(d), leading to the decreased vertical roughness and larger horizontal structure expansion as illustrated in Fig. 2(d1).

To characterize the height distribution, two dimensional (2D) profiles corresponding to each AFM image were generated by taking a linear measurement on the surface, as shown in Fig. 2(a1–d1). The height of biggest pyramid in Fig. 2(a1) is about 2 μm . The root mean square R_q of profiles was used to represent vertical roughness [36]. The R_q value drops from 342.7 nm to 187.5 nm in Fig. 2(a1–d1). The surface enlargement factor was also applied to characterize the surface roughness, defined by $A_F = A_{\text{es}}/A_{\text{ps}}$, where A_{es} is the effective surface area with all valleys and peaks, A_{ps} is the macroscopic base area corresponding to the rectangle area in the AFM observation. The value of A_F is summarized in Table 2.

The cross-sectional FE-SEM images of the prepared rear surface during different etching processes are displayed in Fig. 2(a2–d2), and the measured pyramid facet angle is recorded on each image. Apparently, the random pyramids textured rear surface becomes smoother with increasing the concentration of HF and HNO₃ gradually. In addition, the height of pyramids gets flattened and the pyramid facet angle becomes narrower. The approximate pyramid facet angle α of these samples is fitted to 51.1° , 35.3° , 25.8° and 16.8° from rough to planar. The α values are mainly used to represent different rear surface structures in the OPAL 2 simulations.

The local Al-BSF SEM images of fabricated bifacial PERCs with four different rear surfaces are presented in Fig. 2(a3–d3). It is observed that the Al-Si eutectic layer is uniformly established and few voids are formed, indicating the formation of favorable Al-Si contacts [37,38]. The depth of all the Al-BSFs is around 5 μm , considering that the height of largest pyramids in Fig. 2(a1–d1) is only about 2 μm , thus the rear surface morphology of cells hardly influences the thickness of Al-BSF.

3.2. Impact of rear surface morphology on passivation and optical characteristics

The passivation quality is an extremely important factor for high efficiency solar cells. In order to evaluate the effects of rear surface morphology on passivation property, the τ_{eff} and iV_{oc} of 100 symmetric samples (shown in the inset of Fig. 3(a) with the same morphology and passivation layers on both sides) were measured. It is necessary to explain that the different samples are represented by corresponding A_F values in the following measurements and experimental results. The decreased A_F values indicate that the rear surface structures become smoother. Fig. 3(a) plots the τ_{eff} and iV_{oc} as a function of A_F , both exhibiting a strong correlation of the rear surface morphology. The τ_{eff} increases gradually with decreasing A_F value. The τ_{eff} (166 μs) of samples with an A_F value of 1.068 is almost twice that of 1.621 (92 μs), which is attributed to decreased surface recombination rate and more uniformly deposited passivation films. A similar trend is observed for the iV_{oc} . The iV_{oc} represents the maximal V_{oc} that a completed cell can potentially achieve. Decreasing A_F value from 1.621 to 1.068, the mean iV_{oc} increases from 679.2 mV to 683.8 mV, a gain of up to 4.6 mV could be yielded. The above analysis demonstrates the positive influence of flattened surface on passivation owing to changed crystal orientation, decreased surface area, rounded peaks and troughs, more uniform passivation films. An A_F value below 1.1 is recommended to achieve a good passivation quality of rear surface.

Light trapping has a fundamental impact on the capacity of generating current and greatly depends on the front and rear surface structures of solar cells. Generally, the front surface applies random upright pyramids to absorb light, thus the structures of rear surface will be emphatically studied. To quantify how the rear surface morphology affects the optical characteristics in the targeted bifacial PERCs when

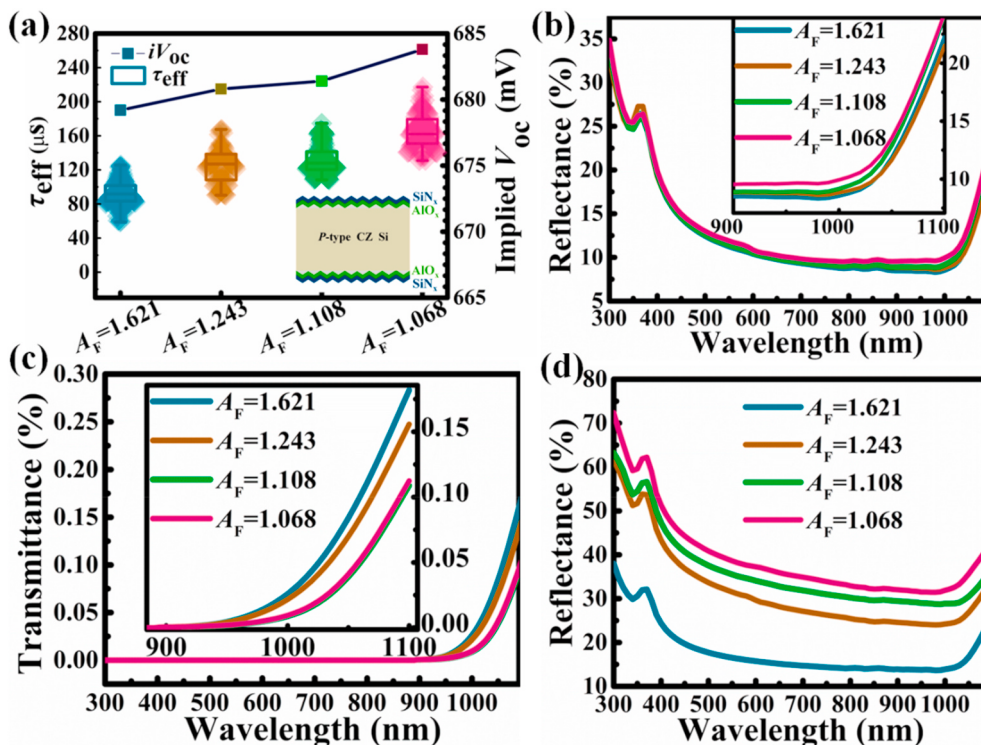
Table 1
The main input parameters for the Quokka 2 simulations.

Region	Quokka 2 parameters	Unit	Value
Main	Cell thickness	μm	170
	Front width	μm	1500
	Rear width	μm	600
	Cell depth	μm	1037
Front (Emitter)	Contact shape	Line	
	Half width	μm	18
	Shape	Full area	
Emitter 1	Sheet resistance	Ω/\square	130
	Junction depth	μm	0.28
	J_{0e}	A/cm^2	7.13E-13
Contact	J_{02}	A/cm^2	0
	Contact resistivity	$\Omega\cdot\text{cm}^2$	1.33E-03
	J_{0e}	A/cm^2	6.50E-14
Non-contact	J_{02}	A/cm^2	0
	Shape	Line	
	Half width	μm	75
Emitter 2	Sheet resistance	Ω/\square	80
	Junction depth	μm	0.35
	J_{0e}	A/cm^2	7.13E-13
Contact	J_{02}	A/cm^2	0
	Contact resistivity	$\Omega\cdot\text{cm}^2$	1.33E-03
	J_{0e}	A/cm^2	1.20E-13
Non-contact	J_{02}	A/cm^2	0
	Bulk	p-type	
	Doping type		
Rear (Base)	Resistivity	$\Omega\cdot\text{cm}$	1.0
	Background lifetime	μs	250
	Contact shape	Rectangle	
BSF 1	Number of contacts	1&3	
	Half width X	μm	16
	Half width Y	μm	250
Contact	Shape	Rectangle	
	Half width X	μm	16
	Half width Y	μm	250
Remaining area	Sheet resistance	Ω/\square	15
	Junction depth	μm	0.8
	$J_{0\text{BSF}}$	A/cm^2	7.33E-13
Non-contact	J_{02}	A/cm^2	0
	Contact resistivity	$\Omega\cdot\text{cm}^2$	2.10E-3
Non-contact	$J_{0, \text{passivated}}$	A/cm^2	1.041E-13 7.347E-14 3.968E-14 2.315E-14

Table 2

Average experimental electrical parameters.

HF/HNO ₃ /H ₂ O			30/150/140	45/240/60	45/240/30	65/240/30
A_F			1.621	1.243	1.108	1.068
$J_{0,\text{passivated}}$ (E-15 A/cm ²)			104.12	73.47	39.68	23.15
Average electrical parameters	5BB	V_{oc} (mV)	Front	677.3	678.6	679.0
			Rear	668.9	670.6	671.3
		J_{sc} (mA/cm ²)	Front	40.29	40.37	40.39
			Rear	31.82	31.08	30.69
		FF (%)	Front	80.69	80.76	80.88
			Rear	81.42	81.53	81.68
		Efficiency (%)	Front	22.02	22.13	22.18
			Rear	17.33	16.99	16.83
		Bifaciality (%)		78.70	76.77	75.88
	9BB	V_{oc} (mV)	Front	677.5	678.8	679.4
			Rear	669.3	671.2	672.1
		J_{sc} (mA/cm ²)	Front	40.66	40.74	40.79
			Rear	32.14	31.37	30.94
		FF (%)	Front	80.83	80.86	80.93
			Rear	81.46	81.59	81.71
		Efficiency (%)	Front	22.27	22.36	22.43
			Rear	17.52	17.18	16.99
		Bifaciality (%)		78.67	76.83	75.75
						74.66

**Fig. 3.** (a) The τ_{eff} and iV_{oc} determined from symmetric samples shown in the inset. (b) Reflectance and (c) transmittance spectra when illuminated from front side with the enlarged parts shown in the inset. (d) Reflectance spectrum when illuminated from rear side.

illuminated from the front side, reflectance and transmittance spectra were measured on semi-device structures (non-metallized and non-passivated of Fig. 1(b) or (c)) in a wavelength range of 300–1100 nm. Fig. 3(b) plots the reflection curve against wavelength for four different A_F values (i.e. different rear surface morphologies). The impact of rear surface is distinct in the wavelength range from 900 nm to 1100 nm. Meanwhile, the performance in short wavelength range is identical, since its reflection is mainly determined by the structures and anti-reflection coatings of front surface, which is the same for these samples. Obviously, the reflection of nearly planar samples ($A_F = 1.068$) exceeds that of the other samples significantly in the long wavelength range, indicating a higher reabsorption of long wavelength photons. Reflection decreases with increasing A_F value. The lowest long wavelength

reflection can be observed for the case of highest value of A_F , and the corresponding surface displays the highest transmission loss in Fig. 3(c), which are detrimental for the re-utilization of long wavelength photons, despite the transmission losses are two orders of magnitude lower than the reflection losses. The two sets with A_F values of 1.108 and 1.068 show similar lower transmittance. The reflection performance when illuminated from rear side was also assessed, as shown in Fig. 3(d). Reflection decreases significantly with increasing A_F value, indicating more trapped photons and higher J_{sc} value.

The above results demonstrate that superior optical performance is achieved on a planar rear surface when light comes from the front side, while worst light trapping ability is also performed on a planar surface when illuminated from the rear side. The optimal rear surface

morphology is uncertain just considering the optical property of semi-device. Hence, the four rear surface morphologies were further integrated into bifacial PERCs to evaluate which rear surface morphology is optimal for bifacial application.

3.3. Characteristics of 5BB bifacial PERCs

The bifacial PERCs featuring different rear surface structures were developed to assess the impact of rear surface on their electrical performance. The bifacial PERCs were measured using a non-reflective black cloth on rear side when light came from front side, the same test method when illuminated from back side. Fig. 4(a) presents the measured front-side and rear-side current density-voltage (J - V) parameters. The V_{oc} steadily increases with the decreased A_F values when illuminated from front side and rear side, as predicted by the trend of iV_{oc} shown in Fig. 3(a). The average V_{oc} of nearly planar samples ($A_F = 1.068$) reaches 680.6 mV, an absolute increment of 3.3 mV compared to the cells with an A_F value of 1.621. The thicker the Al-BSF, the lower the contact recombination, thus higher V_{oc} value of cells [39]. While the thickness of Al-BSF shown in Fig. 2(a3–d3) is independent of rear surface morphology, thus the increased V_{oc} for cells with a lower A_F value can be attributed to the decreased surface area and surface recombination velocity. The difference of 7–8 mV in the observed V_{oc} between front side and rear side will be illustrated by analyzing electrical losses in the following Sec. 3.5. Meanwhile, the J_{sc} exhibits an opposite tendency when illuminated from front side and rear side, improving from 40.29 mA/cm² to 40.51 mA/cm² and decreasing from 31.82 mA/cm² to

30.38 mA/cm² with reducing A_F from 1.621 to 1.068, respectively, which is consistent with preceding reflectance and transmittance spectra analysis in Fig. 3(b–d). The FF values remain a high level of about 81%. For nearly planar samples ($A_F = 1.068$), an average front-side η of 22.26% is achieved, which is 0.24% higher than the cells with an A_F value of 1.621 due to superior passivation quality and improved long-wavelength response. In contrast, the rear-side η value decreases from 17.33% to 16.66% when A_F drops from 1.621 to 1.068, which is ascribed to the sharply decreased J_{sc} values. The relatively lower rear-side η is mainly limited by lower J_{sc} values compared to that of front-side. Under the premise of ensuring excellent rear surface passivation, the J_{sc} value can be further improved by optimizing antireflection property of rear passivation layers. The bifacial PERCs with an A_F value of 1.621 exhibit the highest bifaciality of 78.70%, with a front-side and rear-side η of 22.02% and 17.33%, respectively. The lowest bifaciality of 74.84% is obtained for bifacial PERCs with an A_F value of 1.068. The average electrical parameters of bifacial PERCs with different rear surfaces are summarized in Table 2.

In order to investigate the different electrical performances of the bifacial PERCs with various rear surface morphologies, Fig. 4(b) and (c) show the EQE spectra when the bifacial PERCs are irradiated from front side and rear side, respectively. It can be seen from Fig. 4(b) that the EQE spectra exist difference mainly in the long wavelength range (850–1100 nm) (shown in the inset) but little change in the middle and short wavelength range. This suggests that the different front-side electrical results (Fig. 4(a)) are derived from the rear passivation quality and rear current generation ability, rather than the bulk and emitter region.

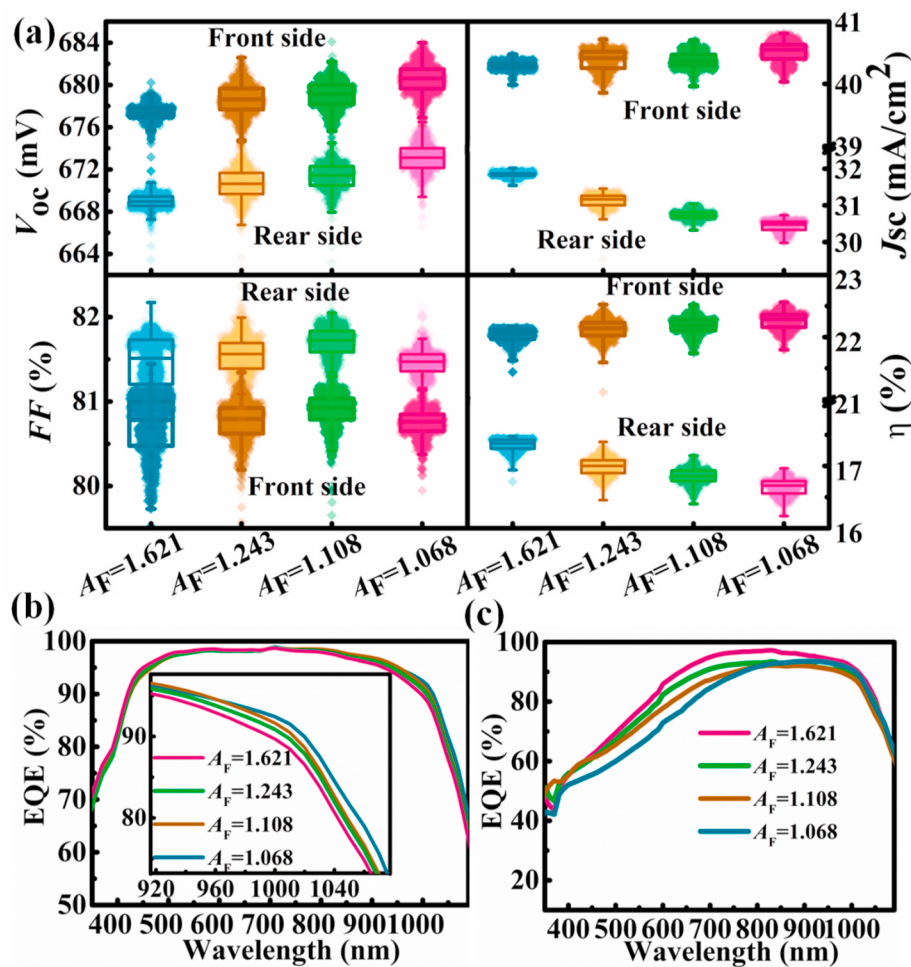


Fig. 4. (a) Experimental J - V parameters including V_{oc} , J_{sc} , FF and η of the fabricated bifacial PERCs with a 5BB design for metal grid (about 800 cells for each group). Measured EQE spectra when illuminated from (b) front-side and (c) rear-side.

Additionally, the trend of EQE spectra in the long wavelength range is in accordance with the experimental V_{oc} and J_{sc} variation in Fig. 4(a). The EQE spectra when illuminated from rear side were also measured as shown in Fig. 4(c). The short-wavelength EQE performance is obviously inferior to that of Fig. 4(b), where the value of EQE approaches 100% in a wide wavelength range. This can be used to illustrate the nearly one fourth lower rear-side J_{sc} values than those of front side. The EQE performance improves significantly with the increased A_F (i.e. increased roughness of rear surface and light trapping ability), which is consistent with the observed rear-side J_{sc} values in Fig. 4(a).

3.4. Electrical results of 9BB bifacial PERCs

MBB technology has attracted considerable attention because of the decreased series resistance and metal shading area [30]. The bifacial PERCs with different rear surface morphologies were also implemented by applying a 9BB design of metal grid. The tested J-V electrical parameters were shown in Fig. 5, the tendency of which is consistent with the results shown in Fig. 4(a), here no further analysis is presented. The increased J_{sc} is observed for 9BB design compared to 5BB one due to shallower shading area and improved carrier collection ability. The series resistance decreases from 2.00 mΩ (5BB) to 1.86 mΩ (9BB), leading to the increase of FF. The bifacial PERCs with an A_F value of 1.068 achieve the highest front-side average efficiency of 22.57% ($V_{oc} = 680.8$ mV, $J_{sc} = 40.95$ mA/cm², FF = 80.96%). A highest bifaciality of 78.67% is obtained for cells with an A_F value of 1.621, with a front-side and rear-side average efficiency of 22.27% and 17.52%, respectively. The electrical results are also summarized in Table 2.

3.5. Electrical loss analysis

The Quokka 2 simulation was performed to theoretically analyze the impact of rear surface structures on electrical losses, and FELA at maximum power point was illustrated. In order to carry out an accurate simulation, the experimental parameters in Table 1, such as junction depth, R_{sh} , $J_{0,emitter}$, $J_{0,contact}$ and so on, were adopted in the simulations. The $J_{0,passivated}$ values extracted from WCT-120 measurements as listed in Table 2 are 104.12, 73.47, 39.68 and 23.15 fA/cm² for cells with an A_F value of 1.621, 1.243, 1.108 and 1.068, respectively. FELA results comprise of recombination losses and resistive losses. According to Fig. 6(a), when light comes from the front side, the recombination loss of

rear passivated area decreases sharply with declined A_F value. When the A_F value is 1.621, the proportion of recombination loss resulted from rear passivated area ranks the third only behind the emitter resistive loss and Shockley-Read-Hall (SRH) recombination loss, while it is negligible as A_F value decreases to 1.068, leading to a decrease of the total efficiency loss.

When the cells are illuminated from rear side, the resistive loss of electron bulk, the recombination losses of SRH and contact at BSF in Fig. 6(b) increase significantly compared to that in Fig. 6(a). Together with the measured EQE spectra in Fig. 4(c), these can be used to explain the 7–8 mV lower rear-side V_{oc} values compared to that of front side. As a result, the efficiency losses of rear side become worse. Moreover, the negative impact of enlarged surface area is more distinct for rear side than front side. When comparing the cells with an A_F value of 1.621 and 1.068, a difference of 1.25 mW/cm² can be deduced for the rear side, while the front side only have a difference of 0.47 mW/cm².

The front-side and rear-side relative η values are also shown for both the 5BB and 9BB design in Fig. 6(c) and (d), respectively, with regarding the cells with an A_F value of 1.621 as the reference. The experimental and simulated front-side conversion efficiency increases gradually as the A_F value decreases, which is consistent with the trend of simulated efficiency loss. In contrast, although a decreased A_F value indicates the better passivation quality, the rear-side conversion efficiency still decreases sharply, this is mainly ascribed to the drastically reduced J_{sc} values. The slight difference between experimental and simulated relative efficiency value can be attributed to several reasons. The thickness of silicon substrate was kept constant in simulations, while it may be influenced by the different etching behaviors. Moreover, the rounding effect in pyramid peaks was ignored, and only the pyramid facet angle was used to represent different rear surface structures.

3.6. Electric energy production simulation

The J-V parameters shown in Fig. 4(a) and Fig. 5 were tested under the standard conditions, with a temperature of 25 °C and irradiance intensity of 1000 W/m², while the irradiance intensity can be varying since the sun goes from east to west over a day. Fig. 7(a) presents the solar spectrum irradiance varying with time on June 22nd in Shanghai. Moreover, the electric energy production of module is strongly associated with the ratio of direct and diffuse light, the albedo of ground and the mounting heights [29], thus simulations of energy yield were

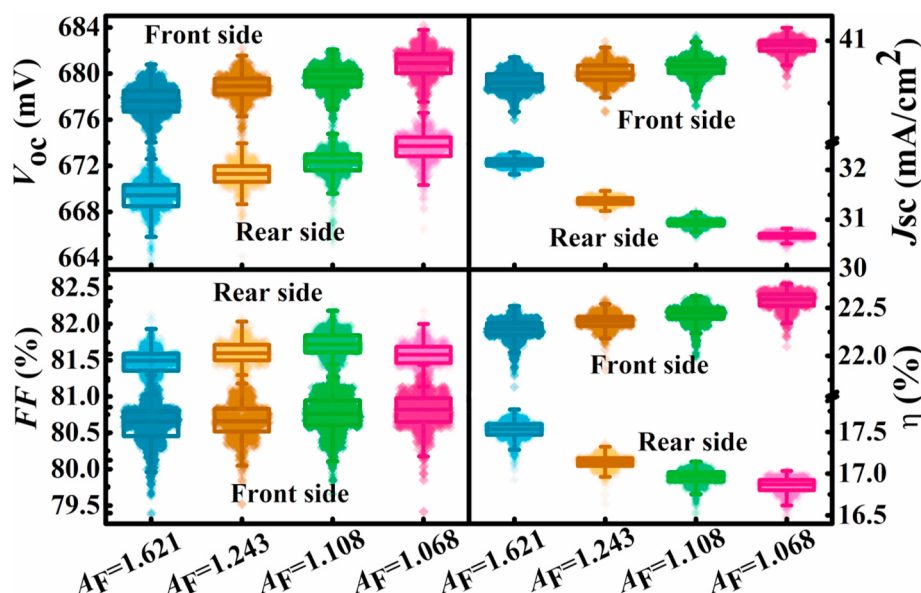


Fig. 5. Experimental J-V parameters of the fabricated bifacial PERCs with a 9BB design for metal grid (about 800 cells for each group).

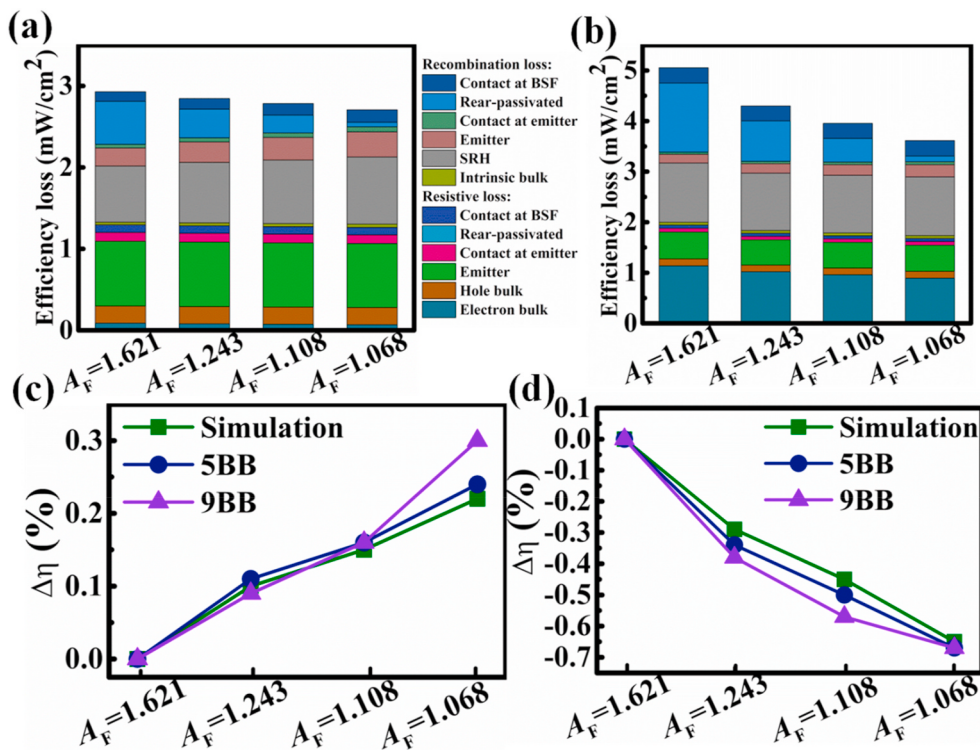


Fig. 6. Simulated FELA results for (a) front-side and (b) rear-side. Simulated and experimental relative efficiency for (c) front-side and (d) rear-side.

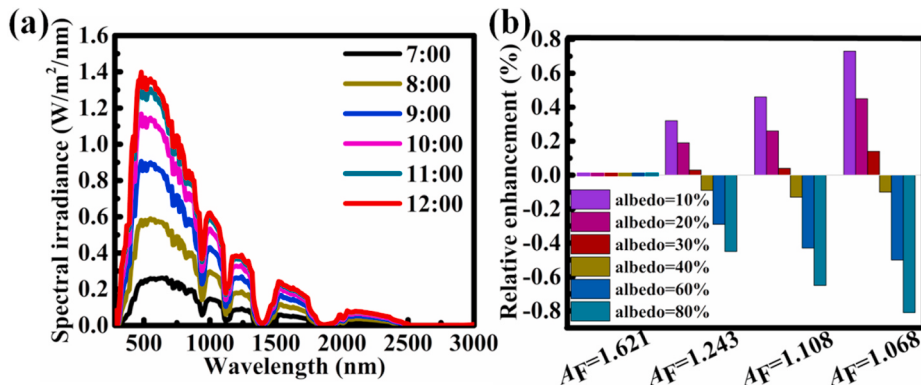


Fig. 7. (a) Solar spectral irradiance at different times in a day. (b) Calculated relative enhancement of energy yield at different ground albedo values, with an A_F value of 1.621 as reference.

indispensable for above fabricated bifacial PERCs to compare their performances in practical applications. Since the bifacial PERCs collect extra diffuse light reflected from the ground, the different ground albedo values depending on module installation surroundings have a significant influence on electric energy generation. Fig. 7(b) shows the calculated relative enhancement of energy production over a day for bifacial PERCs with different A_F values, with regarding the set with an A_F value of 1.621 as reference. When the albedo is 10%, for example, asphalt floor, the lower the A_F value is, the more output energy can be generated. The maximum relative enhancement can reach 0.73% for the solar cells with an A_F value of 1.068. When the modules are located in normal grassland, an albedo of around 20%, the tendency of relative enhancement is similar to the situation of an albedo value of 10%, while the gap among different bifacial PERCs becomes narrower. The solar cells with an A_F value of 1.621, 1.243, 1.108 own comparable electric energy production if the albedo is 30%. When the albedo value further increases to 40% (e.g., sand), the energy generation performance is enhanced with increasing the A_F value. An albedo higher than 40% can be obtained on

white roofing metal, light-gray roofing membrane and white-painted concrete. An albedo of up to 60%–80% is even possible on aluminum foil and snowfield, under this condition an increase in electric energy production of 0.50%–0.81% was predicted for bifacial PERCs with an A_F value of 1.621 compared to that of 1.068.

In summary, the bifacial PERCs with a nearly planar rear surface ($A_F = 1.068$) is recommended if the ground albedo is lower than 30%. The bifacial PERCs with four different rear surfaces can generate comparative electric energy if the albedo is between 30% and 40%. Under the case of albedo higher than 40%, solar cells with rougher rear surface ($A_F = 1.621$) is preferable to apply in such conditions.

4. Conclusions

In conclusion, we have investigated the impact of rear surface morphology on the performance of bifacial p-Si PERCs both experimentally and theoretically. By adjusting the concentration of etching acid solution, the bifacial PERCs with four different rear surface

morphologies were firstly fabricated with a 5BB metal grid. A smoother rear surface has been proved to be advantageous in passivation property, and an increment in front-side V_{oc} of 3.3 mV was achieved with reducing A_F value from 1.621 to 1.068. The invariable thickness of Al-BSF demonstrated that the difference of V_{oc} was independent of rear Al-Si contact. A more flattened rear surface possesses superior optical characteristic due to improved long-wavelength response when illuminated from front side. Meanwhile, a rougher surface is more beneficial when light comes from the rear side attributed to improved light trapping ability. Further integrating these rear surface structures into 9BB bifacial p-Si PERCs, a similar trend was observed. Attributed to the reduced metal shadowing and series resistance, the increased J_{sc} and FF values were obtained for 9BB design compared to 5BB one. Consequently, the cells with an A_F value of 1.068 achieved the highest front-side average efficiency of 22.57%, with a champion efficiency of 22.75% ($V_{oc} = 683.0\text{ mV}$, $J_{sc} = 41.03\text{ mA/cm}^2$, $FF = 81.19\%$). The highest bifaciality of 78.67% was achieved for cells with an A_F value of 1.621, with an average front-side and rear-side efficiency of 22.27% and 17.52%, respectively. Simulated electrical loss analysis indicated that the negative influence of increased $J_{0,\text{passivated}}$ values was more serious for rear-side electrical performance than that of front-side. Finally, by calculating the relative enhancement of energy generation in practical application, the bifacial p-Si PERCs with an A_F value of 1.068 was recommended to install in surroundings with ground albedo lower than 30%. Nevertheless, cells with an A_F value of 1.621 were preferable if the albedo value was higher than 40%.

Declaration of competing interest

The authors declare that they have no known competing financial interests or personal relationships that could have appeared to influence the work reported in this paper.

Acknowledgements

This work was supported by the National Key R&D Program of China (Nos. 2018YFB1500501 and 2018YFB1500302), the National Natural Science Foundation of China (Nos. 11834011 and 11974242), and Shanghai Municipal Key Project of 17DZ1201103. We would like to thank Advanced Electronic Materials and Devices (AEMD) of Shanghai Jiao Tong University for supplying the facility of field emission scanning electron microscopy (FE-SEM).

Appendix A. Supplementary data

Supplementary data to this article can be found online at <https://doi.org/10.1016/j.solmat.2020.110712>.

References

- [1] A.W. Blakers, A. Wang, A.M. Milne, J. Zhao, M.A. Green, 22.8% efficient silicon solar cell, *Appl. Phys. Lett.* 55 (1989) 1363–1365.
- [2] M.A. Green, The passivated emitter and rear cell (PERC): from conception to mass production, *Sol. Energy Mater. Sol. Cells* 143 (2015) 190–197.
- [3] Y. Lv, Y.F. Zhuang, W.J. Wang, W.W. Wei, J. Sheng, S. Zhang, W.Z. Shen, Towards high-efficiency industrial p-type mono-like Si PERC solar cells, *Sol. Energy Mater. Sol. Cells* 204 (2020) 110202.
- [4] <http://taiyangnews.info/technology/longi-24-06-efficiency-perc-cell-world-reco-rd/>.
- [5] K. Krauß, F. Fertig, J. Greulich, S. Rein, R. Preu, BiPERC silicon solar cells enabling bifacial applications for industrial solar cells with passivated rear sides, *Phys. Status Solidi* 213 (2016) 68–71.
- [6] T. Fellmeth, S. Meier, E. Lohmüller, N. Wöhrle, A. Spribile, S. Lohmüller, P. Saint-Cast, A. Wolf, F. Clement, S. Rein, R. Preu, M. Nakahara, M. Dhamrin, H. Knauss, H. Haverkamp, S. Steckemetz, B. Bitnar, T. Weber, P. Palinginis, H. Neuhaus, Industry related approaches for bifacial p-type PERX solar cells, *Jpn. J. Appl. Phys.* 57 (2018), 08RB18.
- [7] T. Dullweber, C. Kranz, R. Peibst, U. Baumann, H. Hannebauer, A. Fülle, S. Steckemetz, T. Weber, M. Kutzer, M. Müller, G. Fischer, P. Palinginis, H. Neuhaus, PERC+: industrial PERC solar cells with rear Al grid enabling bifaciality and reduced Al paste consumption, *Prog. Photovolt. Res. Appl.* 24 (2016) 1487–1498.
- [8] R. Hezel, Novel applications of bifacial solar cells, *Prog. Photovolt. Res. Appl.* 11 (2003) 549–556.
- [9] B. Yu, D.Y. Song, Z.G. Sun, K.M. Liu, Y. Zhang, D.D. Rong, L.J. Liu, A study on electrical performance of n-type bifacial PV modules, *Sol. Energy* 137 (2016) 129–133.
- [10] R. Guerrero-Lemus, R. Vega, T. Kim, A. Kimm, L.E. Shephard, Bifacial solar photovoltaics-A technology review, *Renew. Sustain. Energy Rev.* 60 (2016) 1533–1549.
- [11] H. Park, S. Chang, S. Park, W.K. Kim, Outdoor performance test of bifacial n-type silicon photovoltaic modules, *Sustainability* 11 (2019) 6234.
- [12] H. Mori, Radiation energy transducing device, US Patent 35 (1966) 40748.
- [13] A. Kalio, A. Richter, C. Schmiga, M. Glatthaar, J. Wilde, Study of dielectric layers for bifacial n-type silicon solar cells with regard to optical properties, surface passivation quality, and contact formation, *IEEE J. Photovolt.* 4 (2014) 575–580.
- [14] H.B. Huang, C. Modanese, S.H. Sun, G. von Gastrow, J.B. Wang, T.P. Pasanen, S. Li, L.C. Wang, Y.M. Bao, Z. Zhu, S. Sneed, H. Savin, Effective passivation of p⁺ and n⁺ emitters using SiO₂/Al₂O₃/SiN_x stacks: surface passivation mechanisms and application to industrial p-PERT bifacial Si solar cells, *Sol. Energy Mater. Sol. Cells* 186 (2018) 356–364.
- [15] L. Janßen, H. Windgassen, D.L. Bätzner, B. Bitnar, H. Neuhaus, Silicon nitride passivated bifacial Cz-silicon solar cells, *Sol. Energy Mater. Sol. Cells* 93 (2009) 1433–1439.
- [16] D. Rudolph, T. Buck, A. Teppe, F.B. Masouleh, R. Harney, Firing through aluminum grid paste for bifacial solar cells, *Energy Proc.* 92 (2016) 971–977.
- [17] J. Kim, J. Kim, J.Y. Lim, Y. Hwang, J. Cho, H. Choi, E. Lee, Laser ablation of aluminum oxide and silicon nitride rear-side passivation for i-PERC cell, *Renew. Energy* 79 (2015) 135–139.
- [18] <https://itrvp.vdma.org/documents/27094228/29066965/ITRPV02020.pdf>;ba3d a187-3186-83de-784e-6e3b10d96f3f.
- [19] G.L. Lu, F. Zheng, J.Q. Wang, W.Z. Shen, Thin Al₂O₃ passivated boron emitter of n-type bifacial c-Si solar cells with industrial process, *Prog. Photovolt. Res. Appl.* 25 (2017) 280–290.
- [20] F. Kiefer, J. Krügener, F. Heinemeyer, M. Jestremski, H.J. Osten, R. Brendel, R. Peibst, Bifacial, fully screen-printed n-PERT solar cells with BF₂ and B implanted emitters, *Sol. Energy Mater. Sol. Cells* 157 (2016) 326–330.
- [21] M. Taguchi, A. Yano, S. Tohoda, K. Matsuyama, Y. Nakamura, T. Nishiwaki, K. Fujita, E. Maruyama, 24.7% record efficiency HIT solar cell on thin silicon wafer, *IEEE J. Photovolt.* 4 (2014) 96–99.
- [22] L.F. Yang, S.H. Zhong, W.B. Zhang, X.B. Li, Z.P. Li, Y.F. Zhuang, X. Wang, L. Zhao, X.M. Cao, X.M. Deng, Q. Wang, W.Z. Shen, Study and development of rear-emitter Si heterojunction solar cells and application of direct copper metallization, *Prog. Photovolt. Res. Appl.* 26 (2018) 385–396.
- [23] W.L. Wu, Z.W. Zhang, F. Zheng, W.J. Lin, Z.C. Liang, H. Shen, Efficiency enhancement of bifacial PERC solar cells with laser-doped selective emitter and double-screen-printed Al grid, *Prog. Photovolt. Res. Appl.* 26 (2018) 752–760.
- [24] C. Schwab, A. Wolf, M. Graf, J. Nekarda, G. Kästner, M. Zimmer, S. Kühnhold, M. Hofmann, D. Biro, R. Preu, Passivation of inline wet chemically polished surfaces for industrial PERC devices, *Energy Proc.* 27 (2012) 573–579.
- [25] C. Kranz, S. Wyczanowski, U. Baumann, K. Weise, C. Klein, F. Delahaye, T. Dullweber, R. Brendel, Wet chemical polishing for industrial type PERC solar cells, *Energy Proc.* 38 (2013) 243–249.
- [26] C. Kranz, B. Wolpensinger, R. Brendel, T. Dullweber, Analysis of local aluminum rear contacts of bifacial PERC+ solar cells, *IEEE J. Photovolt.* 6 (2016) 830–836.
- [27] T. Dullweber, N. Wehmeier, A. Nowack, T. Brendemühl, S. Kajari-Schröder, R. Brendel, Industrial bifacial n-type silicon solar cells applying a boron co-diffused rear emitter and an aluminum rear finger grid, *Phys. Status Solidi* 213 (2016) 3046–3052.
- [28] N. Wöhrle, T. Fellmeth, J. Greulich, B. Bitnar, H. Neuhaus, P. Palinginis, R. Köhler, S. Rein, Understanding the rear-side layout of p-doped bifacial PERC solar cells with simulation driven experiments, *Energy Proc.* 124 (2017) 225–234.
- [29] T. Dullweber, H. Schulte-Huxel, S. Blankemeyer, H. Hannebauer, S. Schimanke, U. Baumann, R. Witteck, R. Peibst, M. Köntges, R. Brendel, Y. Yao, Present status and future perspectives of bifacial PERC+ solar cells and modules, *Jap. J. Appl. Phys.* 57 (2018), 08RA01.
- [30] S. Braun, G. Micard, G. Hahn, Solar cell improvement by using a multi-busbar design as front electrode, *Energy Proc.* 27 (2012) 227–233.
- [31] A. Fell, A free and fast three-dimensional/two-dimensional solar cell simulator featuring conductive boundary and quasi-neutrality approximations, *IEEE Trans. Electron Devices* 60 (2013) 733–738.
- [32] M. Müller, G. Fischer, B. Bitnar, S. Steckemetz, R. Schiepe, M. Mühlbauer, R. Köhler, P. Richter, C. Kusterer, A. Oehlke, E. Schneiderlöchner, H. Sträter, F. Wolny, M. Wagner, P. Palinginis, D.H. Neuhaus, Loss analysis of 22% efficient industrial PERC solar cells, *Energy Proc.* 124 (2017) 131–137.
- [33] S.H. Zhong, W.J. Wang, M. Tan, Y.F. Zhuang, W.Z. Shen, Realization of quasi-omnidirectional solar cells with superior electrical performance by all-solution-processed Si nanopyramids, *Adv. Sci.* 4 (2017) 1700200.
- [34] Y.F. Zhuang, S.H. Zhong, X.J. Liang, H.J. Kang, Z.P. Li, W.Z. Shen, Application of SiO₂ passivation technique in mass production of silicon solar cells, *Sol. Energy Mater. Sol. Cells* 193 (2019) 379–386.
- [35] A. Dastgheib-Shirazi, M. Steyer, J. Junge, S. Gindner, G. Hahn, A study of the surface morphology of silicon: effect of parasitic emitter etching on the rear-side performance of silicon solar cells, in: 25th European Photovoltaic Solar Energy Conference and Exhibition/5th World Conference on Photovoltaic Energy Conversion, Valencia, Spain, 2010.

- [36] M. Richter, P. Saint-Cast, T. Dannenberg, M. Zimmer, J. Rentsch, Impact of rear side roughness on optical and electrical properties of a high-efficiency solar cell, *Energy Proc.* 77 (2015) 832–839.
- [37] T. Lauermann, B. Fröhlich, G. Hahn, B. Terheiden, Diffusion-based model of local Al back surface field formation for industrial passivated emitter and rear cell solar cells, *Prog. Photovolt. Res. Appl.* 23 (2015) 10–18.
- [38] R. Horbelt, G. Hahn, R. Job, B. Terheiden, Void formation on PERC solar cells and their impact on the electrical cell parameters verified by luminescence and scanning acoustic microscope measurements, *Energy Proc.* 84 (2015) 47–55.
- [39] C. Kranz, U. Baumann, B. Wolpensinger, F. Lottspeich, M. Müller, P. Palinginis, R. Brendel, T. Dullweber, Void formation in screen-printed local aluminum contacts modeled by surface energy minimization, *Sol. Energy Mater. Sol. Cells* 158 (2016) 11–18.